



Nanoscale

Colloidal Plasmonic Nanostar Antennas with Wide Range Resonance Tunability

Journal:	<i>Nanoscale</i>
Manuscript ID	NR-ART-07-2019-006533.R2
Article Type:	Paper
Date Submitted by the Author:	09-Sep-2019
Complete List of Authors:	Tsoulos, Theodoros; University of Patras, Department of Physics; Rutgers University, Materials Science and Engineering Atta, Supriya; Rutgers University, Chemistry and Chemical Biology Lagos, Maureen; Rutgers The State University of New Jersey, Materials Science and Engineering Beetz, Michael; Ludwig-Maximilians-Universitat Munchen, Batson, Philip; Rutgers, Physics and Astronomy Tsilomelekis, George; Rutgers The State University of New Jersey, ; Rutgers Fabris, Laura; Rutgers University, Materials Science and Engineering

SCHOLARONE™
Manuscripts

Colloidal Plasmonic Nanostar Antennas with Wide Range Resonance Tunability

Ted V. Tsoulos,¹ Supriya Atta,² Maureen J. Lagos,^{1,3} Michael Beetz,⁴ Philip E. Batson,^{1,3} George Tsilomelekis,⁵ and Laura Fabris*¹

¹ Department of Materials Science and Engineering, Rutgers University, 607 Taylor Road
Piscataway NJ 08854, United States.

² Department of Chemistry and Chemical Biology, Rutgers University, 610 Taylor Road
Piscataway NJ 08854, United States.

³ Department of Physics & Astronomy, Rutgers University, 136 Frelinghuysen Road, Piscataway
NJ 08854.

⁴ Department of Chemistry and Center for NanoScience (CeNS), Ludwig Maximilians
Universität München, 81377 Munich, Germany.

⁵ Department of Chemical and Biochemical Engineering, Rutgers University, 98 Brett Road,
Piscataway NJ 08854, United States.

KEYWORDS: localized surface plasmon resonances, colloidal nanostars, plasmon tunability, 3D
nano-antennas, EELS

ABSTRACT

Gold nanostars display exceptional field enhancement properties and tunable resonant modes that can be leveraged to create effective imaging tags, phototherapeutic agents, and hot electron-based photocatalytic platforms. Despite having emerged as the cornerstone among

plasmonic nanoparticles with respect to resonant strength and tunability, some well-known limitations have hampered their technological implementation. Herein we tackle these recognized intrinsic weaknesses, which stem from the complex, and thus computationally untreatable, morphology and the limited sample monodispersity, by proposing a novel 6-spike nanostar, which we have computationally studied and synthetically realized, as the epitome of 3D plasmonic nanoantenna with wide range plasmonic tunability. Our concerted computational and experimental effort shows that these nanostars combine the unique advantages of nanostructures fabricated from the top-down and those synthesized from the bottom-up, showcasing a unique plasmonic response that remains largely unaltered in going from the single particle to the ensemble. Furthermore, they display multiple, well-separated, narrow resonances, the most intense of which extends in space much farther than observed before for any plasmonic mode localized around a colloidal nanostructure. Importantly, the unique close correlation between morphology and plasmonic response leads the resonant modes of these particles to be tunable between 600 and 2000 nm, a unique feature that could find relevance in cutting edge technological applications.

INTRODUCTION

Gold nanostars have shown to possess plasmonic properties with the potential to enable technological breakthroughs in various fields, such as imaging,¹ sensing,² and catalysis.³ Importantly, their limited cytotoxicity⁴ promises to enable their use *in vitro* and *in vivo*. With respect to their applicability, their most appealing features are the tunability of the resonant modes associated with the spikes well into the near infrared (NIR) and the generation of intense scattered electric fields at the tips of the spikes upon interaction with impinging radiation. These

features, in addition to the unique tridimensional morphology that these nanoparticles possess when synthesized colloidally, render gold nanostars a very promising nanomaterial onto which implementing assembly-free 3D plasmonic antennas. Substantially hampering this development are however the well-known multi-spiked complex morphology, which is difficult to rationally control during synthesis or to fundamentally study with computation, and the largely poly-dispersed batches that are obtained even following seed-mediated protocols, notwithstanding some recent progress⁵. Recently we have shown⁶ that spike length tunability, sample monodispersity, and batch-to-batch reproducibility can be achieved for gold nanostars when following a seed-mediated method employing both AgNO_3 and Triton X as the shape inducing reagents. In our work we have also shown that the morphological stability (especially of the tips) can be furthered by increasing the relative amounts of AgNO_3 , which appears to be stabilizing the as-synthesized nanostar by depositing as a monolayer of metallic Ag throughout the nanostructure, as demonstrated by high resolution STEM-EDX. With further improvements upon our initial results, this novel, 6-spiked nanostar is well poised to become a useful plasmonic nanoantenna with intrinsic 3D tunability, with relevance not only from the applied standpoint but also as a model nanoparticle for fundamental studies. The rationale behind this claim is two-fold: 1) Separated spikes will likely only weakly couple within a single nanostar, rendering their resonances easy to study and interpret, and 2) spikes with high shape anisotropy should display multiple narrow harmonics of a fundamental plasmonic mode, as our calculations predict⁷ (and as observed in long nanorods and nanowires)⁸. Motivated by these appealing features, in this work, referring back to the 2007 seminal paper by Hao *et al.*,⁹ we investigate in detail, with a holistic computational-experimental approach, the relationship between nanostar morphology and relevant plasmonic properties, focusing in particular 1) on determining how structural

modulation is reflected into the tunability of the various LSPR modes and 2) on colloiddally synthesizing nanostars whose ensemble optical response matches, within a narrow range of variability, their single particle characteristics. In doing so, we aim to prove this nanostar as the missing link between bottom-up and top-down nanomaterials, providing (in 3D) the low cost and ease of fabrication that are unique of the former, and the refined tunability and monodispersity that characterize the latter. As added bonuses, these nanostars display (*vide infra*) plasmonic resonances within a wide range spanning the visible, the NIR, and the short wave infrared (SWIR), and a first harmonic mode that extends in space much farther than observed with any resonances in other plasmonic nanomaterials, rendering them uniquely suited for applications in which mode coupling is sought on large scale arrays.

Contrary to nanostar systems, which have until now only found minimal technological relevance, gold nanorods and nanowires have been successfully studied and understood, and they are now well-established nanomaterials leveraged for technological applications. The clear structure-property relationships that describe their plasmonic behavior has led to their use for the study of localized and propagating plasmons^{10, 11} and to demonstrate the concept of wave-particle duality.¹² Regardless of the notable improvement in the synthetic protocols, that now achieve monodispersed nanorods with high tunability,¹³ and the decrease in plasmon band width through post-synthetic manipulations,¹⁴ the 1D morphology of nanorods and nanowires limits their ability to probe the tridimensional space, unless 3D self-assembly protocols are employed¹⁵. By realizing that nanostars represent the epitome of a 3D plasmonic antenna and by taking as example the progress achieved over the years with nanorods, we herein carried out single-particle and ensemble characterization to validate structure-property predictions enabled by our 3D finite element modeling method. In particular, we demonstrate numerically the presence of

an intense fundamental mode in the SWIR regime and its higher harmonics at lower energy, and we demonstrate its existence on highly monodispersed nanostar samples obtained with our synthetic protocol. Furthermore, we show that this fundamental mode can be accurately measured via ATR-FTIR in dense nanostar samples, if 3D interparticle coupling of tips and cores is taken into account. Importantly, we prove the existence of this mode via STEM-EELS at resonant energies almost unaltered from what spectrophotometrically measured in ensemble, offering some interesting insight into the opportunity to compare plasmon mode excitation mediated by photons or electrons in aloof-beam configurations. Finally, we determine that the position of the various harmonic modes linearly depends on the length of the spikes, a dependence that is maintained both at the single particle and the ensemble level. Importantly, by tomographically reconstructing the 3D morphology of an almost ideal and a rather defective nanostar, and by inserting the topographic elements in the finite elements model, as we reported before¹⁶, we prove that it is indeed only by synthesizing highly monodisperse nanostars that we can experimentally confirm in ensemble the results obtained computationally and experimentally at the single particle level. We believe that this work, with the thorough insight it offers, could provide the necessary knowledge basis to achieve an improved understanding of the plasmonic properties of these highly anisotropic nanomaterials and promote their implementation in technologically-relevant applications.

RESULTS AND DISCUSSION

By employing 3D finite element optical simulations *via* the Comsol Multiphysics software (see Supporting Information for details), we have implemented a computational framework to study the plasmonic properties of gold nanostars in which the core and the spikes

are considered to resonate as *inseparable* units, thus contributing interactively to the number, position, and intensity of the resulting LSPR modes⁷. We focused on the study of our recently reported 6-branch gold nanostars⁶, i.e. 3D colloidal nanostructures characterized by conical spikes with high shape anisotropy and lengths between 70 and 100 nm, radially grown on decahedral cores via a Triton X 100-based seed-mediated protocol, and decorated by small hemispherical tips (**Figure 1**). These morphologically simple systems reveal some interesting plasmonic properties, in particular the role of the long spikes on the overall plasmonic response, which can be confirmed experimentally both at the ensemble and single particle level. Importantly, the exquisite morphological tunability and batch monodispersity lend themselves well to establishing these nanostars as 3D colloidal nanoantennas with a unique plasmonic response that can be studied both at the single particle and ensemble level without loss of information, if not for minor peak broadening.

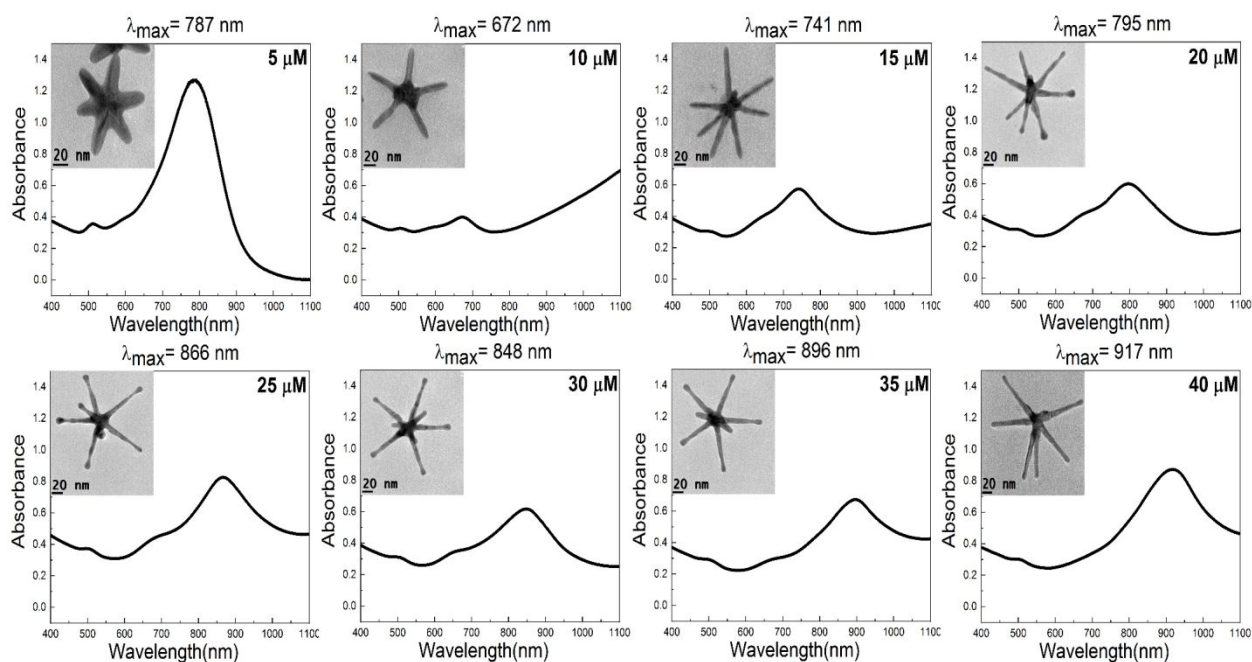


Figure 1. Transmission electron micrographs and UV-Vis-NIR spectra of gold nanostar samples obtained by increasing the amount of AgNO_3 between 5 and 40 μM as described in the Methods section. The resulting UV-Vis-NIR spectra are characterized by a prominent LSPR mode that shifts between 672 nm (at 10 μM AgNO_3 concentration) and 917 nm (at 40 μM AgNO_3 concentration) and can be described as the second harmonic of the primary dipolar mode, which resonates above 1100 nm and thus cannot be observed in these spectra. For the 5 μM AgNO_3 concentration case, the observed prominent band is the first harmonic mode, which in this case appears at higher energies because of the shorter spike length obtained at this AgNO_3 concentration. It is important to observe how the morphology of the nanostars, and of the spikes in particular, changes in close correlation to the amount of AgNO_3 added. Scale bars at 20 nm.

Our model of the optical response predicts, for idealized models of these nanostars, the existence of an intense resonant band at wavelengths longer than 1000 nm (at positions that depend on the specific nanostar morphology), that can be assigned to the first harmonic of the localized surface plasmon resonance (LSPR) spike mode. As expected, higher order harmonics (*i.e.* second and third) are also predicted, that resonate between 600 and 1000 nm, with spacing between the three that depends on the slant length of the conical spikes. Our model also predicts a linear dependence between the position of the harmonic modes and the spike length. In order to

test our model on real gold nanostar samples and corroborate its predictions, we synthesized 6-branch gold nanostars employing our seed-mediated protocol in which the concerted action of Triton X, ascorbic acid, and silver nitrate enables to synthesize gold nanostars with spike lengths between 70 nm and 100 nm (which we will later also refer to as average size) and characterized by LSPR bands that can be tuned, through the addition of increasing amounts of AgNO_3 (see **Figure 1**),¹⁷ from 600 to 2000 nm. The possibility to bridge the gap between computation and experiment with a truly 3D model that does not make constraining structural assumptions, promises to lead to a complete understanding of structure-plasmonic property relationships in these complex nanomaterials. We have investigated in depth the size and shape dependence of the plasmon resonances for the synthesized 6-branched nanostars, reporting in **Figure S1** the results for particles with spike lengths between 70 nm and 100 nm. Size and shape can be tuned by rationally varying the relative concentrations of AgNO_3 , ascorbic acid, Triton X, and seeds, as well as reaction time (**Figure S2**). Furthermore, detailed dimensional analysis over samples larger than 100 particles revealed substantial monodispersity (both within and among batches), with maximum standard deviations of $\pm 4\%$, as reported in the representative histograms in **Figure S1 (i-l)**. Analysis of nanostar morphology has also shown that, although some of the nanostars possess five or seven spikes, the majority of them are characterized by six branches, as confirmed by detailed TEM tomography reconstruction¹⁶.

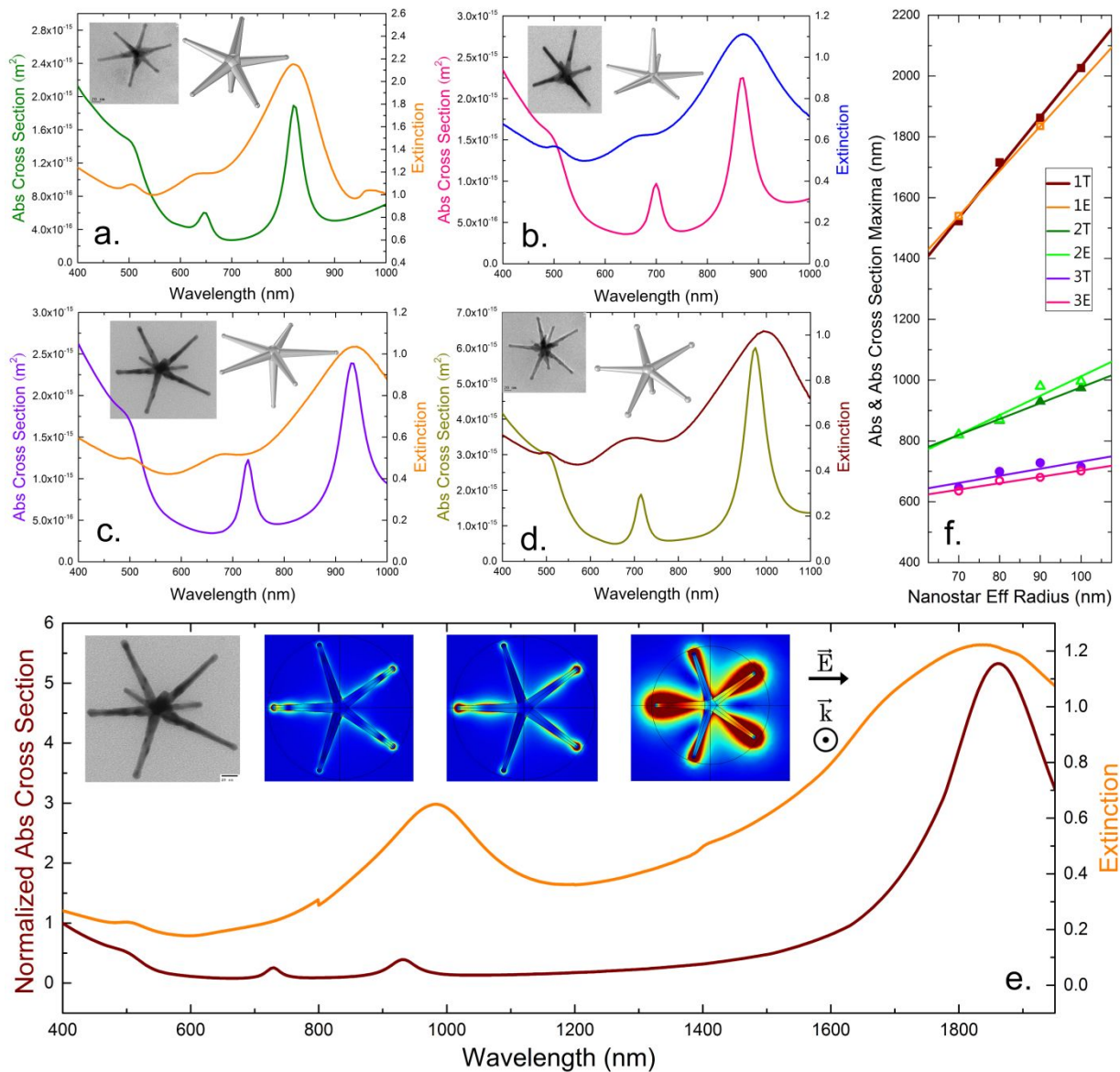


Figure 2. Experimental and computational spectra of 6-spike nanostars of a) 70, b) 80, c) 90, and d) 100 nm spike lengths. e) Long range theoretical and experimental spectra of 90 nm radius 6-spike nanostars. E-field norm (calculated *via* Eq. 5 in Methods section) maps of the first, second, and third harmonic modes at 1865 nm, 930 nm, and 730 nm, respectively. Spectra normalization was carried out with respect to the photon energy of each wavelength compared to the photon energy at 400 nm. FWHM for first and second harmonic are 242 nm and 65 nm, respectively, for the calculated spectra, and 500 nm and 190 nm, respectively, for the experimental ones. f) Linear dependence (actual fits) between the harmonic modes resonant maxima (1, 2, and 3) and the nanostar spike lengths. Note the decreasing slope as we move towards higher harmonics and the very good matching between theoretical (T) predictions and experimental (E) results. Details on the normalization of Figure 3e are reported in **Figure S3**.

UV-Vis-NIR-SWIR spectrophotometry was employed to optically characterize in ensemble 6-branch nanostar samples with spike lengths of 70 nm, 80 nm, 90 nm, and 100 nm (**Figure 2**), showing excellent agreement between the results predicted by our optical model on ideal nanostars (Figure 2 a-d); in particular, the very good agreement between the position and normalized intensity of the bands modeled and measured (Figure 2e and **Figure S3**) confirms the validity of our model. Importantly, the experimental validation corroborates our generalized vision⁷ of plasmonic resonances in gold nanostars as harmonics of the main LSPR mode, whose appearance as distinct bands can be achieved only in the presence of long spikes with high shape anisotropy. When nanostars with shorter and thicker spikes are studied, the higher harmonics, being less intense and more closely spaced compared to the case of nanostars with high aspect ratio spikes, seemingly disappear giving rise to the well-known broad LSPR bands observed for surfactant free gold nanostars.^{18, 19} In reality these resonances become simply enveloped within the more intense fundamental mode. Inter-spike coupling, common in the case of multi-spike nanostars (again observed in surfactant free gold nanostar syntheses) also causes them to slightly blue shift, further broadening the LSPR band. Importantly, disruptions in nanostar morphology lead to substantial modifications in the plasmonic response, as shown in **Figure S4**. We confirmed this computational prediction by collecting TEM tomograms of two individual gold nanostars of 72 and 76 nm spike length, one of which characterized by a close-to-ideal morphology (72 nm), and the other (76 nm) being rather imperfect (**Figure 3**), and transferring the topographic elements into Comsol Multiphysics, as we reported before¹⁶. Correct reconstruction was confirmed through ortho slices in the x, y, and z directions, as reported in **Figure S5**. The approach allowed us to simulate the absorption cross sections and scattered E-fields for the real nanostars in 3D and to directly compare the fidelity and accuracy of our

modeling approach for ideal nanostars versus their real counterparts. The direct comparison of

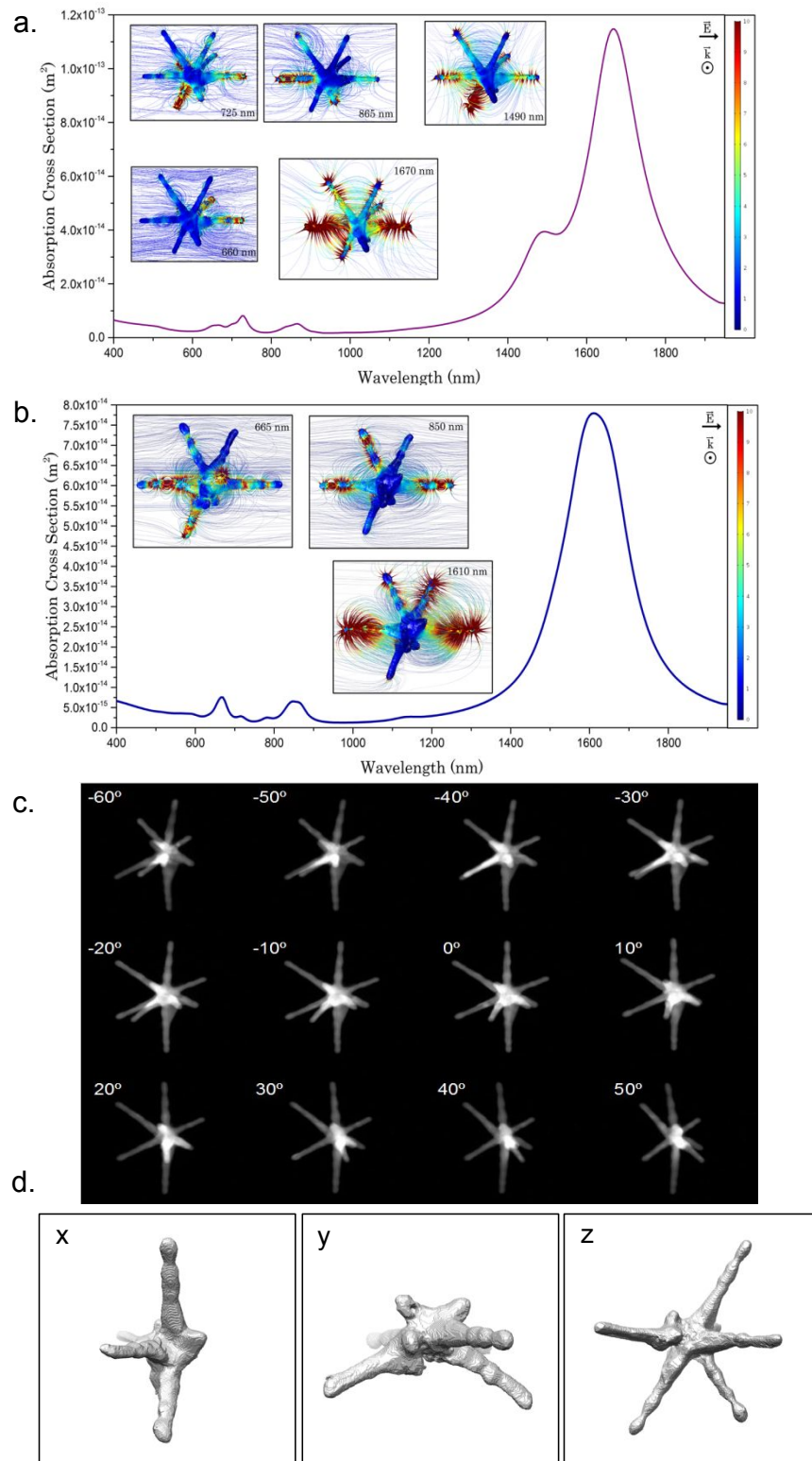


Figure 3. Numerical solutions for the E-field norm of two different nanostars 3D reconstructed from TEM tomograms. a) a highly defective one with spikes of variable length and a more ideal nanostar in b) with spikes of equal length (despite the presence of a short unformed spike). Presented at the eigenvalues of the main resonant modes, these real 3D reconstructed nanostars yield a behavior that solidifies our approach. A slightly imperfect nanostar in the a) case exhibits additional resonances in all of the three reported harmonic cases, two of which, i.e. a secondary 1st and secondary 3rd harmonic, are depicted in the E-field norm plots. Streamline plots allow us to visualize the resonances in real particles like these. In both cases small protrusions on the volume of the stars contribute to broadenings and slight asymmetries on the peaks, although the spectral response is clear for the more ideal nanostar in b), corroborating our approach and supporting our computational data for disrupted geometries (Figure S4). Interestingly, very small differences in spike lengths result in clear secondary resonances, which stands as a proof that our synthetic method yields highly monodisperse and reproducible samples and our numerical approach successfully describes even slight disruptions in the geometry and the resulting spectral profile. In c) STEM tilt series collected for nanostar in b) for tomographic reconstruction. The topographic elements were then employed to transfer the real nanostar morphology into Comsol Multiphysics and model absorption cross sections and scattered E fields in 3D, as we reported before¹⁶. d) Projections in x, y, and z directions of the 3D tomographic reconstruction realized from the tilt series reported in b).

the calculated spectra for the imperfect (Figure 3a) and the more ideal (Figure 3b) nanostar highlights the presence, in the first case, of various secondary resonances appearing as satellites of the main resonant modes, and assignable to the LSPR resonances of shorter nanostar spikes. Interestingly, the main harmonic mode at ca. 1650 nm shows a prominent side peak that corresponds to the first harmonic of the LSPR of a much shorter spike (notice the ca. 200 nm blue shift). This secondary first harmonic band does not appear for the more ideal nanostar in b) where, while the shape and FWHM of the band are indicative of the merging of two different bands, the spikes are all more similarly sized thus resonating at very similar energies. By also comparing the second and third harmonics, it is clearly evident that the defective spikes in a) lead to the generation of several more resonant bands as compared to the case in b), which will, for the limit case of a nanostar with tens of spikes of variable lengths (such as the surfactant free nanostars) eventually convolute to form a single broad LSPR band. The similarity between the

calculated spectra between ideal and real nanostars, reinforces the validity of our computational calculations on ideal 6-branch nanostars as an effective predictor of the resonances of real nanostars, provided that a reproducible and tunable synthetic method for the growth of the nanostar is employed to ensure sufficient monodispersity. Our study, proposing a more generalized approach to the interpretation of LSPR bands in gold nanostars, predicts very well the position of the harmonics based on the detailed morphology of the nanostar in exam. The core dimensions, the length, and the sharpness of the spikes, along with the tip morphology (**Figure S6**), dictate the position and distance between the harmonics. The relative position of the bands governs the linear relationship reported in Figure 2f, and follows a simplified rule in agreement with antenna theory.²⁰ In the long range 400-1950 nm spectrum in Figure 2e we report both the Vis-NIR-SWIR spectrum and the calculated normalized absorption cross section of a 90 nm nanostar, along with three E-field maps highlighting the spatial distribution of the field at the position of the *maxima* for the three observed harmonics. The very good agreement between position and intensity modeled and experimentally measured provides a solid experimental proof of the validity of our computational approach, which is further supported by the ATR-FTIR and EELS results presented onwards. Interestingly, our optical model suggests that the first harmonic mode, in addition to displaying substantially higher intensity compared to its higher harmonics, appears to extend in space much farther from the surface than the other two, which could be leveraged in techniques such as surface enhanced Raman scattering (SERS) where E-field enhancements lead to higher signal intensity and assay sensitivity.

Figure 2 also highlights a very unique aspect of the nanostars we report, that is the extension of their resonant window well into the SWIR. We thus hypothesized that a linear dependence between the resonance wavelength and nanostar spike length could be measured also

employing FTIR. A validation of this hypothesis would render these particles extremely powerful as plasmonic nanoantennas for applications in medical imaging, sensing, or catalysis, in addition to potentially acting as fiducial marks for resonance alignment of UV-Vis-NIR spectrophotometry and FTIR. In **Figure 4**, we present the ATR-FTIR spectra of highly concentrated aqueous solutions of gold nanostars with spike lengths spanning between 70 nm and 100 nm. The full spectral range, 700-7500 cm^{-1} , is reported in **Figure S7**. In the 4000 – 6500 cm^{-1} spectral range, we observe the peak *maxima* for the first harmonic to be centered at ~5700 cm^{-1} , 5180 cm^{-1} , 4930 cm^{-1} , and 4830 cm^{-1} for the 70, 80, 90, and 100 nm respectively. The peak positions of the four different samples fit nicely the E-field norm introduced by the numerical predictions and the Vis-NIR-SWIR spectroscopy measurements. A noticeable shift in the observed first harmonic peaks can be attributed to interparticle coupling effects (**Figure S8**), since the FTIR measurements took place in concentrated solutions as compared to the Vis-NIR spectrophotometric measurements, as supported by our recent computational work on 3D nanostar antenna coupling⁷. Interestingly, the observed center of each peak appears to be linearly dependent on the average size of the gold nanostars in solution, demonstrating the strong dependence of this plasmonic mode on the length of the spike, as described in the previous section and plotted in Figure 4d and 4e.

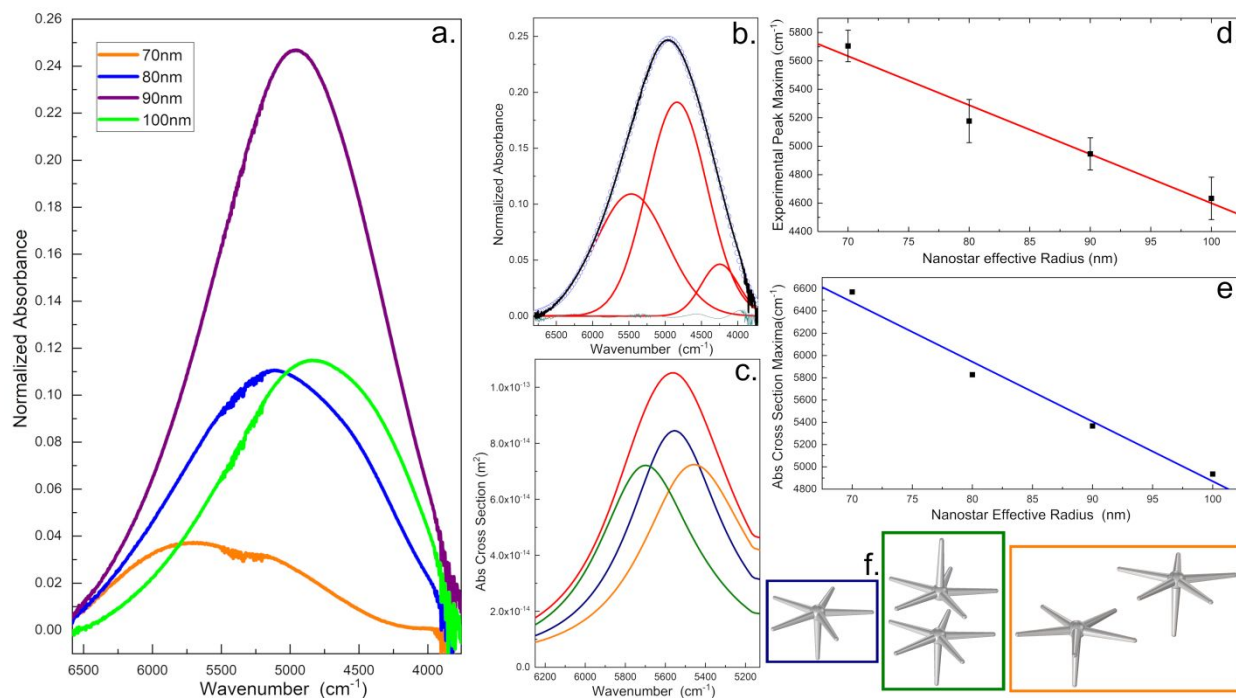


Figure 4. FTIR spectra collected on nanostars with 70 nm, 80 nm, 90 nm, and 100 nm spike lengths. Normalization carried out with respect to the area under the curve of each spectrum (a). Spectrum of a suspension of nanostars with 90 nm spike length deconvoluted with Gauss function (b). Theoretical absorption cross section spectra of 1) a single 90 nm nanostar, 2) two nanostars with their in-plane spikes kept parallel at 50 nm distance, 3) two nanostars aligned tip-to-tip at 50 nm, along with the average of these three spectra shown in red (c and f). Linear fitting of the observed FTIR peak maxima shows a strong interdependence between the first harmonic resonances and the spike length experimentally (d) and theoretically (e). Error bars in d) calculated from peak deconvolution, as reported in **Figure S9**.

The results obtained from the ATR-FTIR spectra further underscore the ability and reliability of the developed protocol for the synthesis of colloidal nanostars with plasmonic properties that can be rationally tailored for specific applications. It is worth mentioning here that contrary to the well-defined, Gaussian-type peaks predicted by the model, in our ATR-FTIR spectra the first harmonic appears to be a convolution of more than one contribution in the overall spectral envelope. To address this issue, all the spectra were deconvoluted using Gauss functions based on the Levenberg–Marquardt algorithm as shown elsewhere.^{21–24} The deconvoluted spectra show two or three major peaks separated by approximately 800 cm^{-1} . To

further investigate the latter, in Figure 4b and 4c we report the comparison between the deconvoluted ATR-FTIR spectrum and the calculated absorption cross section for 90 nm-spike nanostars. The distinct peaks in ATR-FTIR can be attributed to the same plasmonic mode under different geometrical configurations (Figure 4f). Numerical results (Figure 4c and 4f) show that changing the distance as well as the configuration between two adjacent nanostars can both blue shift and red shift the plasmonic mode. The computational treatment to nanostar coupling aims to outline the importance of considering multiple geometric configurations between randomly dispersed adjacent nanostars at high concentrations when interpreting the experimental results. We have investigated three of these numerous possible configurations and report the shifts of the first harmonic with respect to the distance between nanostars (Figure S8).

After demonstrating that our calculations can accurately predict, given the spike length, the resonances of real 6-branch gold nanostars employing an idealized 6-branch model nanostar, and demonstrating that the predicted resonances can be validated by measuring them in ensemble by simply employing UV-Vis-SWIR spectrophotometry or ATR-FTIR, we confirmed, at the single particle level, the observed results by carrying out electron energy loss spectroscopy (STEM-EELS) measurements on an individual 90 nm-spike nanostar. While single particle scattering data could be in first principle proposed to assess the plasmonic response, the presence of the substrate, coupling anisotropically to the nanostars, would have further complicated the experimental response, and was therefore not deemed accurate to assess the LSPR bands in this particular study.

Figure 5 exhibits EELS spectra acquired on a 6-spike nanostar with the electron beam probing the nanostructure in non-intersecting and intersecting geometries. Since the plasmon coupling between spikes is very weak due to their large physical separation,²⁵ one can in

principle analyze their plasmonic behavior considering an isolated spike coupled to the star core. This approach allows us to probe a single spike and then repeat the process for the other spikes of the stars. It's important to mention that in this experiment the examined nanostar was supported by an amorphous carbon film with 15 nm thickness; in these conditions it is expected

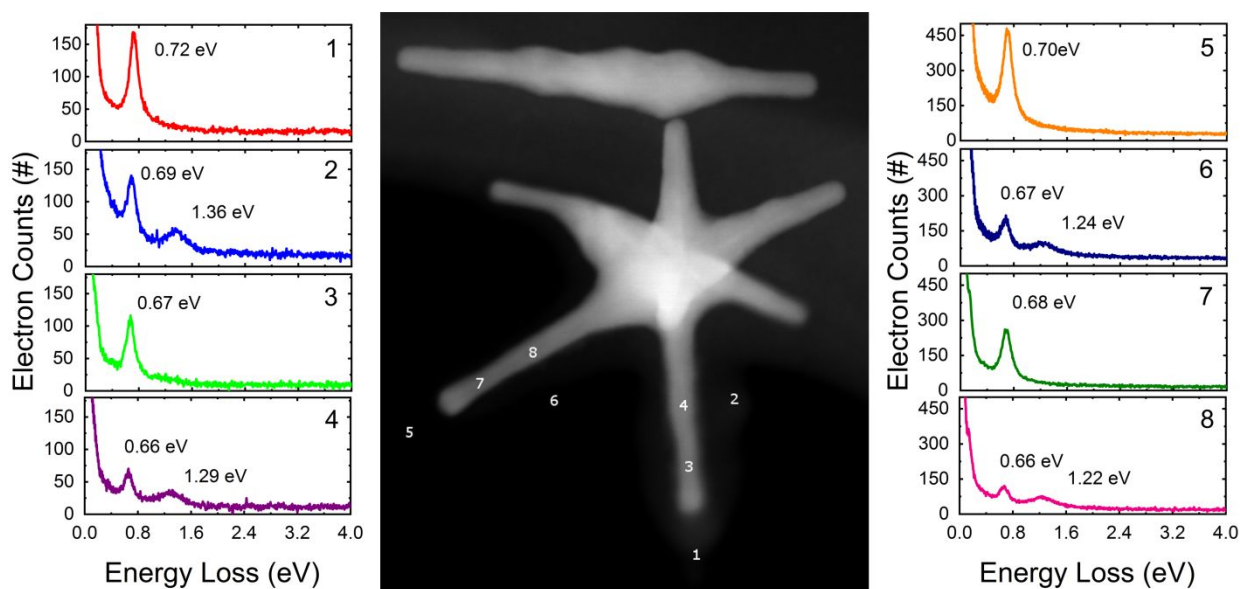


Figure 5. EELS spectra collected at the positions depicted in the STEM micrograph presented in the middle. Up to two resonances associated with the first (670 meV) and second (1360 meV) harmonic excitations can be observed, with slight energy shifts that depend on the proximity to the core of the position probed by the electron beam. This nanostar was chosen for EELS analysis because the two probed spikes were observed to be oriented almost perpendicularly with respect to the carbon-coated TEM grid, thus ensuring that the interference of the substrate, although substantially smaller in the NIR compared to the UV-visible region, would be further minimized.

that the interference of the C film on the EELS response will be minimal, especially in the energy regime probed. We obtained the same findings for all the spikes, as illustrated in Figure 5 (left side–spike 1; right side–spike 2). Note that the spectra can exhibit up to two resonances associated with the first (670 meV) and second (1360 meV) harmonic excitations, depending on the beam location (the third harmonic mode is not intense enough to be measured). The resonant energies are similar to those found by optical techniques (UV-Vis-NIR and ATR-FTIR, Figures

3 and 4 respectively) and match well the computational simulations of the optical response. While we recognize that comparing mode excitation via electron beam and plane wave illumination involves different physical phenomena, we can consider the connection between electron and photon excitation to be valid in the aloof mode for large input parameters (*i.e.*, when the electron beam does not intersect the nanostructure). In intersecting geometry, on the other hand, two phenomena occur: a) The electron beam can probe coupled core-spike resonances with sufficient sensitivity to measure shifts due to the varying electron density, which increases as we move from the tip to the base of the spike; b) The electron beam perturbs the local electron density leading to resonant mode damping. When the electron beam is located in regions near/within the tip (position 1, 3) the excitation of the first harmonic dominates the EELS spectra. This is expected due to the dipolar configuration of that mode in rod-like structures,²⁶ which is highly efficiently excited in the non-intersecting configuration (position 1). It is also important to note that there is a slight shift to lower energies of the characteristic resonance of the first harmonic, as we move along the axis of the spike (position 3). We also probed the middle regions of the spikes producing an additional excitation at around 1290 meV, which corresponds to the excitation of the second harmonic. A blue-shift trend can be observed for the resonances excited, as we move from the middle regions of the spikes to their extremities and to the aloof mode. When the beam intersects with the spikes it disturbs the local charge distribution, which gives rise to the mentioned damping of the spike modes, leading to a red shift, notable in the case of the first harmonic as the beam moves from the aloof mode to the inner part of the spikes.

CONCLUSIONS

In conclusion, the 6-branched nanostars reported herein offer an example of highly anisotropic, colloiddally-synthesized plasmonic material in which the optical properties of the nanostructure can be predicted computationally and observed experimentally owing to their high monodispersity. While other non-spherical nanoparticles (*e.g.* nanorods) have been synthesized with high degree of monodispersity and synthetic control, the morphology of these nanostars is substantially more complex to achieve. However, the opportunity to leverage them as true 3D nanoantennas, is a powerful rationale to further our understanding of their properties. In-depth multi-technique characterization has shown that the peak positions of the plasmonic resonances linearly depend on the length of the spikes, with slight variations originating from the specific tip- and spike-morphologies. The proposed model has predicted a strong plasmonic mode, along with its higher order eigenmodes, in excellent detail. EELS data, collected on isolated spikes, have confirmed the influence of the electrons of the core on the spectral position of the various harmonics; in addition, they have underscored the importance of taking into consideration the effect of the electron beam in intersecting probing geometries. From the single particle level to the highly interacting ensemble, the agreement between optical model and experiment advocates for the need of a combined approach towards a rational and effective evolution of plasmonic materials and methods. The high monodispersity and batch-to-batch reproducibility of the samples, ensured by our synthetic protocol, suggest that these 6-branched nanostars might be ideal testbeds for the experimental validation of plasmonics theory or for the implementation of plasmonics-based technology in medical imaging, sensing, or catalysis.

METHODS

Synthesis of 6 branched stars with tunable plasmon resonance. 6-branched stars with tunable

plasmon resonance were synthesized by modifying the concentration of AgNO_3 , starting from the general protocol, described as follows. A seed solution was prepared by addition of a freshly prepared ice-cold solution of NaBH_4 (0.6 ml, 0.01 M) into a solution mixture of HAuCl_4 (10 ml, 0.25 mM) and 0.15 M Triton X. The solution turned immediately from pale yellow to orange after addition of NaBH_4 . A 14 μL aliquot of seeds was added to the growth solution containing 20 ml of 0.15 M of Triton-X, 0.4 ml of 25 mM HAuCl_4 , 0.04 ml of 0.788 M ascorbic acid, and a AgNO_3 solution whose concentrations were ranging from 5 to 40 μM (Figure 1). The reaction mixture was gently stirred at room temperature for 10 minutes. The final nanostar suspension was purified by centrifugation at 4,000 g for 10 min and re-dispersed with 5 ml of Ultrapure MilliQ water (18.2 $\text{M}\Omega\text{-cm}$).

Instrumentation.

UV-Vis-NIR Spectrophotometry. Absorption spectra were recorded on a Thermo Scientific Evolution 300 UV-Vis spectrophotometer using a quartz cuvette with 1 cm path. A Cary Series UV-Vis-NIR Spectrophotometer (Cary 5000 UV-Vis-NIR) was used to collect the UV-Vis-NIR spectra. 1 mm quartz cuvette was used with double beam mode to get the UV-Vis-NIR spectrum.

Transmission Electron Microscopy. Nanoparticle morphology was determined using a Topcon 002B transmission electron microscope depositing the nanoparticle suspension on Ted Pella Inc. PELCO TEM grids.

ATR-FTIR Spectroscopy. A Thermo Fisher iS50 FTIR spectrometer equipped with a deuterated, L-alanine-doped triglycine sulfate (DLATGS) detector, and a Golden Gate single-

reflection diamond ATR was used for all spectroscopic studies. The instrument was equipped with a purge gas of dehumidified air (Parker-Balston 75-45) to remove water vapor. The resolution of the instrument was set at 4 cm^{-1} for the whole set of measurements and the number of scans varied from 16 to 32. For each measurement, $\sim 100\ \mu\text{l}$ of the gold nanostar aqueous solution were placed on the ATR crystal and left there for 5 mins to settle. The spectra were collected at 25°C by using air as reference background.

Electron Energy Loss Spectroscopy. A Nion high energy resolution monochromated EELS-STEM (HERMES™) with 60 keV acceleration voltage was employed to collect the reported EELS data.²⁷ Experimental conditions of high-beam current probes were used, typically attained with a condenser-lens setting, favoring higher beam current over spatial resolution. The spatial resolution was kept between $1.5\ \text{\AA}$ and $2.0\ \text{\AA}$. The EELS spectrometer entrance aperture subtends a 20-mrad ($2.5\ \text{\AA}^{-1}$) half-angle at 60 kV. The EELS spectra were acquired in the aloof and intersecting geometries over 500 ms and 1s, respectively, with 20 meV energy resolution. Plasma cleaning and mild heat treatment at 75°C for six hours were employed to pretreat the sample to eliminate the surfactant layer and avoid carbon contamination under the electron beam.

STEM Tomography. Scanning transmission electron microscopy (STEM) was carried out using a FEI Titan Themis transmission electron microscope (TEM) operated at 200kV. Energy dispersive X-ray spectroscopy maps (EDX maps) were obtained in a scanning mode of TEM (STEM). The point resolution in this aberration-corrected mode is 0.08nm. 1nm resolution EDX maps with an average beam current of 100pA are routine with this microscope. STEM tomography was obtained collecting a tilt series (from -60° to $+60^\circ$ in 10° steps) using a FEI Titan Themis 60-300 operated at 300 kV. Tomographic

reconstruction was obtained using a software based on TomToolbox for Matlab²⁸. Alignment of the tilt series was carried out via TomoJ²⁹. Masked SIRT and DART was performed according to Zürner et al.³⁰. Discrete tomography of demanding samples was based on a modified SIRT algorithm³⁰.

Nanostar Synthesis

Materials. Gold (III) chloride trihydrate ($\text{HAuCl}_4 \cdot 3\text{H}_2\text{O}$), silver nitrate (AgNO_3 ; 99.995%), L(+)-ascorbic acid, sodium borohydride (NaBH_4), and TritonX-100 were purchased from Sigma-Aldrich. All these chemicals were used without further purification. Ultrapure MilliQ water (18.2 $\text{M}\Omega \cdot \text{cm}$) was used in all syntheses. All glassware was aqua regia cleaned before each synthesis.

Synthesis of 6 Branched Gold Nanostars. 6-branched gold nanostars were synthesized following a modified seed-mediated method first developed by Taglietti and coworkers.¹⁷ Briefly, the seed solution was prepared by adding 0.6 ml of a fresh, ice-cold 0.01 M NaBH_4 solution to a mixture containing 0.1 ml of 25 mM HAuCl_4 and 10 ml of 0.15 M Triton X. After addition of NaBH_4 the solution turned immediately from pale yellow to orange-red. The mixture was stirred for 2 minutes and aged for 10 minutes at 4 °C before use. The growth solution was prepared by adding 40 μl of 0.788 M ascorbic acid to a solution containing 0.4 ml of 25 mM HAuCl_4 , and 20 ml of 0.15 M of Triton-X. A variable amount of AgNO_3 solution was added to the growth solution to obtain a precise spike length: For instance, 45, 50, 60, and 100 μM AgNO_3 were used for the synthesis of the 80, 70, 90, and 100 nm spike length, respectively. After that, a variable amount of seeds were added to the growth solution. Specifically, nanostars with 70 nm spike length were synthesized by addition of 24 μl (14 μl for the other three spike

lengths) seed solutions to the growth solution. The color of the solution turned from colorless to green after addition of the seeds, with the color becoming more intense after 5 minutes. The solution was gently stirred at room temperature for 12 hours. The conical spike morphology with spherical tip was obtained when 25 μM AgNO_3 were added to the growth solution, and the reaction time was 10 minutes. The rod morphology was obtained when 15 μM AgNO_3 was added to the growth solution, and the reaction time was 10 minutes. The solution was purified via centrifugation at 4,000 g for 10 min and redispersed with 5 ml of Ultrapure MilliQ water (18.2 $\text{M}\Omega\cdot\text{cm}$).

Case Example: Synthesis of 80 nm spike length stars. 6-branched gold nanostars with 80 nm spike length were synthesized by addition of a 14 μL aliquot of seed solution to the growth solution containing 20 ml of 0.15 M of Triton-X, 0.4 ml of 25 mM HAuCl_4 , 0.04 ml of 0.788 M ascorbic acid, and 45 μM AgNO_3 solution. An intense brown color appeared immediately after addition of the seeds. The solution was gently stirred at room temperature for 12 hours until it became green in color. The suspension was purified by centrifugation at 4,000 g for 10 min and re-dispersed with 5 ml of Ultrapure MilliQ water (18.2 $\text{M}\Omega\cdot\text{cm}$).

Spike Length Measurement of Gold Nanoparticles. The core diameter, spike length, and aspect ratio of nanostars were measured *via* ImageJ software. The spike length was measured from the center of the core to the tip of the spike. We have measured 150 spikes for each different type nanostar to generate the reported statistics.

ASSOCIATED CONTENT

Supporting Information

Details of the modeling method and additional details of the synthetic protocols. Details on the normalization method for absorption cross section spectra, and modeling results when disruptions are introduced in the geometry. A graph and discussion on the monodispersity of the synthesized colloids, full range ATR-FTIR spectra, and analytical description of the coupling between nanostars under three different geometric configurations. ATR-FTIR peak deconvolution for all collected data.

CONFLICTS OF INTEREST

There are no conflicts of interest to declare.

ACKNOWLEDGMENTS

This work was funded by the National Science Foundation Grant CHE-1415881.

AUTHOR INFORMATION

Corresponding Author

*E-mail: lfabris@soe.rutgers.edu

Phone: +1-848-445-5606

REFERENCES

1. M. W. Rotz, K. S. B. Culver, G. Parigi, K. W. MacRenaris, C. Luchinat, T. W. Odom and T. J. Meade, *ACS Nano*, 2015, **9**, 3385-3396.
2. A. S. D. S. Indrasekara, S. Meyers, S. Shubeita, L. C. Feldman, T. Gustafsson and L. Fabris, *Nanoscale*, 2014, **6**, 8891-8899.
3. A. Sousa-Castillo, M. Comesaña-Hermo, B. Rodríguez-González, M. Pérez-Lorenzo, Z. Wang, X.-T. Kong, A. O. Govorov and M. A. Correa-Duarte, *The Journal of Physical Chemistry C*, 2016, **120**, 11690-11699.
4. M. Bhamidipati and L. Fabris, *Bioconjugate Chemistry*, 2017, **28**, 449-460.
5. A. S. De Silva Indrasekara, S. F. Johnson, R. A. Odion and T. Vo-Dinh, *ACS Omega*, 2018, **3**, 2202-2210.
6. S. Atta, M. Beetz and L. Fabris, *Nanoscale*, 2019, **11**, 2946-2958.

7. T. V. Tsoulos and L. Fabris, *The Journal of Physical Chemistry C*, 2018, **122**, 28949-28957.
8. O. Nicoletti, M. Wubs, N. A. Mortensen, W. Sigle, P. A. van Aken and P. A. Midgley, *Opt. Express*, 2011, **19**, 15371-15379.
9. F. Hao, C. L. Nehl, J. H. Hafner and P. Nordlander, *Nano Letters*, 2007, **7**, 729-732.
10. C. Rewitz, T. Keitzl, P. Tuchscherer, J.-S. Huang, P. Geisler, G. Razinskas, B. Hecht and T. Brixner, *Nano Letters*, 2012, **12**, 45-49.
11. E. K. Payne, K. L. Shuford, S. Park, G. C. Schatz and C. A. Mirkin, *The Journal of Physical Chemistry B*, 2006, **110**, 2150-2154.
12. L. Piazza, T. T. A. Lummen, E. Quiñonez, Y. Murooka, B. W. Reed, B. Barwick and F. Carbone, *Nature Communications*, 2015, **6**, 6407.
13. N. Ortiz, B. Zoellner, S. J. Hong, Y. Ji, T. Wang, Y. Liu, P. A. Maggard and G. Wang, *ACS Applied Materials & Interfaces*, 2017, **9**, 25962-25969.
14. G. González-Rubio, P. Díaz-Núñez, A. Rivera, A. Prada, G. Tardajos, J. González-Izquierdo, L. Bañares, P. Llombart, L. G. Macdowell, M. Alcolea Palafox, L. M. Liz-Marzán, O. Peña-Rodríguez and A. Guerrero-Martínez, *Science*, 2017, **358**, 640-644.
15. C. Hamon, M. Postic, E. Mazari, T. Bizien, C. Dupuis, P. Even-Hernandez, A. Jimenez, L. Courbin, C. Gosse, F. Artzner and V. Marchi-Artzner, *ACS Nano*, 2012, **6**, 4137-4146.
16. T. V. Tsoulos, L. Han, J. Weir, H. L. Xin and L. Fabris, *Nanoscale*, 2017, **9**, 3766-3773.
17. P. Pallavicini, A. Dona, A. Casu, G. Chirico, M. Collini, G. Dacarro, A. Falqui, C. Milanese, L. Sironi and A. Taglietti, *Chemical Communications*, 2013, **49**, 6265-6267.
18. Y. Hsiangkuo, G. K. Christopher, H. Hanjun, M. W. Christy, A. G. Gerald and V.-D. Tuan, *Nanotechnology*, 2012, **23**, 075102.
19. M. Chirea, S. S. E. Collins, X. Wei and P. Mulvaney, *The Journal of Physical Chemistry Letters*, 2014, **5**, 4331-4335.
20. B. Paolo, H. Jer-Shing and H. Bert, *Reports on Progress in Physics*, 2012, **75**, 024402.
21. D. Fischer, P. Pötschke, H. Brünig and A. Janke, *Macromolecular Symposia*, 2005, **230**, 167-172.
22. A. G. Kalampounias, G. Tsilomelekis and S. Boghosian, *Journal of Molecular Liquids*, 2014, **198**, 299-306.
23. A. G. Kalampounias, G. Tsilomelekis and S. Boghosian, *J Chem Phys*, 2015, **142**, 154503.
24. P. Pötschke, H. Brünig, A. Janke, D. Fischer and D. Jehnichen, *Polymer*, 2005, **46**, 10355-10363.
25. S. Mazzucco, N. Geuquet, J. Ye, O. Stéphan, W. Van Roy, P. Van Dorpe, L. Henrard and M. Kociak, *Nano Letters*, 2012, **12**, 1288-1294.
26. M. Bosman, E. Ye, S. F. Tan, C. A. Nijhuis, J. K. W. Yang, R. Marty, A. Mlayah, A. Arbouet, C. Girard and M.-Y. Han, *Scientific Reports*, 2013, **3**, 1312.
27. L. K. Ondrej, C. L. Tracy, F. M. Matthew, S. Gwyn, E. B. Philip and D. Niklas, *Journal of Physics: Conference Series*, 2014, **522**, 012023.
28. S. Nickell, F. Förster, A. Linaroudis, W. Del Net, F. Beck, R. Hegerl, W. Baumeister and J. M. J. J. o. s. b. Plitzko, 2005, **149**, 227-234.
29. C. Messaoudi, T. Boudier, C. O. S. Sorzano and S. J. B. b. Marco, 2007, **8**, 288.
30. A. Zürner, M. Döblinger, V. Cauda, R. Wei and T. Bein, *Ultramicroscopy*, 2012, **115**, 41-49.

TABLE OF CONTENT GRAPHIC for “Colloidal Plasmonic Nanostar Antennas with Wide Range Resonance Tunability”, by Ted V. Tsoulos, Supriya Atta, Maureen J. Lagos, Michael Beetz, Philip E. Batson, George Tsilomelekis, and Laura Fabris.

Gold nanostars with six branches and high shape anisotropy can be optically modeled and synthesized with high monodispersity providing a truly tridimensional plasmonic nanoantenna.

